ACS NANO

www.acsnano.org

Quantitatively Profiling the Evolution of Hydrogen Storage and Defect Healing Processes in Palladium at the Nanoscale

Yu-Cheng Chiu, Bo-Yi Chen, Chin-Chia Hsu, Chia-Wei Tsai, Shih-Ming Wang, I-Ling Chang, and Chih-Wei Chang*

Cite This: *ACS Nano* 2025, 19, 10070−10077

Read Online

ACCESS | Metrics & More | Article Recommendations | Supporting Information

ABSTRACT: **Light elements or compounds with an average atomic number (Z) of less than 10 are difficult to detect due to their weak interactions with electrons and photons. Here, we introduce a direct thermal absorbance measurement platform for scanning electron microscopy. The technique, named ZEM, is particularly sensitive to low Z materials, including hydrogen (Z = 1) and vacancy (Z = 0). We use Pd as an example to explore ZEM's potential in characterizing hydrogen storage materials. ZEM reveals that hydrogen storage is highly inhomogeneous, concentrating on grain boundaries and defects. ZEM also unveils a large defect density created by hydrogenation, uncovering abundant voids beneath the surface. ZEM's nondestructive detection method allows us to investigate multiple hydrogen charging−discharging cycles, revealing two distinct hydrogen uptake phenomena accompanied by unusual defect healing processes. We further establish the causality between hydrogenation and defect formation, quantifying distinct correlations between hydrogen-induced defect generation and defect-mediated hydrogen trapping. The rich phenomena discovered by the ZEM underscore its potential in material characterizations, particularly for light elements or compounds.**

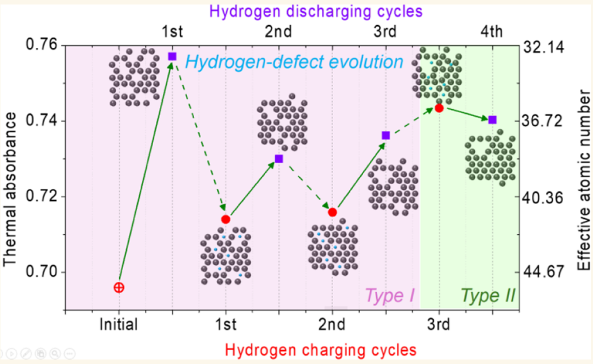

KEYWORDS: *hydrogen storage, palladium, defects, light elements, electron microscopy*

INTRODUCTION

One of the fundamental challenges in developing a hydrogen economy is reducing the technical barriers to characterizing hydrogen-related phenomena.[1,2] These include the physics and chemistry of hydrogen embrittlement,[3,4] hydrogen trapping at interfaces or defects,[5,6] and hydrogen spillover occurring at the nanoscale.[7−10] However, very few tools are available to meet the requirement.[11,12] Sievert or gravimetric techniques employ pressure or weight measurements to determine hydrogen absorption/desorption of bulk materials and generally do not exhibit spatial resolution. Thermal desorption spectroscopy (TDS) can detect hydrogen desorption at sub-ppm levels but cannot distinguish the signals' spatial variations.[11,12] Neutron scattering can probe the structure of hydrides or hydrogen diffusion dynamics using diffraction techniques, but it cannot characterize samples smaller than millimeters.[11] Secondary ion mass spectroscopy (SIMS) can localize the hydrogen in a material with ~100 μm lateral resolution and ~0.1 μm depth resolution.[13] However, because SIMS is a destructive method, it cannot be used to study hydrogen evolution for multiple charging−discharging cycles. Atom probe tomography (APT) requires dedicated sample preparation procedures to improve the spatial resolution of hydrogen detection to the nanoscale, but it also relies on a destructive method.[5,6,14] On the other hand, because one can easily focus an electron beam beyond the diffraction limit of light, material characterizations at the nanoscale are usually carried out by various electron microscopy techniques. However, standard tools like electron probe microanalysis equipped with wavelength dispersive X-ray spectroscopy cannot detect elements with $Z < 3$.[15,16] Fundamentally, the weak interaction between hydrogen atoms and the probe makes nanoscale characterization difficult.

Received: November 23, 2024
Revised: February 23, 2025
Accepted: February 26, 2025
Published: March 4, 2025

https://doi.org/10.1021/acsnano.4c16841

Compared to techniques for detecting the hydrogen content, even fewer tools are capable of quantifying the vacancy concentration. Archimedes' method relies on microbalance and only applies to bulk samples.[17] The differential thermal expansion method relies on precise measurements of $3(\Delta L/L - \Delta a/a)$ where $\Delta L/L$ is the temperature-dependent thermal expansion, and $\Delta a/a$ is lattice constant variation.[18] It has been a technique exclusive to bulk materials until recently.[19] On the other hand, vacancy detection based on positron annihilation spectroscopy (PAS) relies on the longer lifetime of positrons when interacting with vacancies.[20] However, the estimation of vacancy concentration relies on the parameters of trapping rate models and accessing a focused positron beam has remained challenging. Thus, the spatial resolution of PAS could reach ~50 μm so far.[21]

Here, we address both challenges using a single new technique. As shown in Figure, 1(a and b), we have recently introduced a direct thermal absorbance measurement platform within a scanning electron microscope (SEM) and discovered that the majority of the absorbed energy is converted to heat, i.e., A_{th}/A = 98%,[22,23] where A is the absorbance and A_{th} is the thermal absorbance. Because other forms of absorbance, such as X-ray, cathodoluminescence, or electron beam absorbed current, would contribute the remaining ~2% of A, we have $A_{\text{th}} \approx 1 - R$ when the transmittance of electrons is zero ($T = 0$) in a system. That is, A_{th} is nearly complementary to R. Thus, $1 - A_{\text{th}}$ can be regarded as an ideal backscattering electron (BSE) detector with ~2% systematic error. As shown in Figure 1c, the above statement has been experimentally verified for materials with atomic numbers (Z) ranging from 1 to 79. We have demonstrated that this technique can determine the effective Z (Z_{eff}) of a sample.[23] Unlike BSE detectors, which have weak responses to light elements or compounds, our ZEM technique is particularly sensitive to low Z materials due to its signal being complementary to that of an ideal BSE detector. ZEM also eliminates many uncertainties associated with BSE detectors and can serve as a standardization tool.[24] This work will explore ZEM's potential in characterizing hydrogen storage materials.

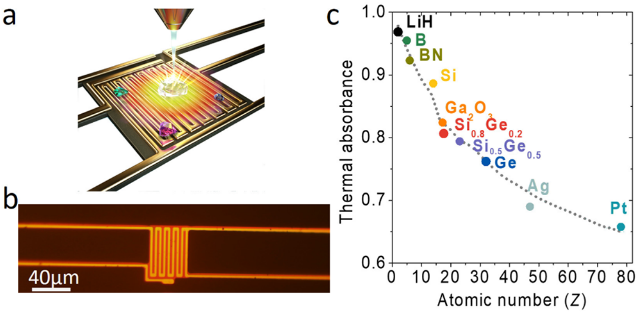

Figure 1. Direct thermal absorbance measurement platform and the operation of ZEM. (a) A schematic figure of a direct thermal absorbance measurement platform with samples inspected under an electron beam. (b) An optical image of the platform consisting of a patterned Pt thermometer supported by suspended SiN_x beams. (c) The experimental data of A_{th} (solid color symbols, obtained from our earlier work[23]). The results of the CASINO simulation for A_{th} (red dash-dotted curve) under a V_{acc} = 5 kV electron beam are also shown for comparison.

RESULTS/DISCUSSION

Quantifying Hydrogen Storage at the Nanoscale. As shown in Figure 1a,b, the ZEM measurement platform is like a bolometer. It consists of a suspended SiN_x membrane with patterned Pt wires on it. The linear resistance vs temperature of the Pt wire can serve as a thermometer to measure the temperature variation when an electron beam raster scans the sample deposited at the bolometer. An electron beam acceleration voltage (V_{acc}) to satisfy the T = 0 condition can be estimated by employing Monte Carlo simulation using the CASINO program.[25−27] Using a stoichiometric Si_3N_4 nanowire as calibration, the uncertainty of A_{th} is estimated to be ±1%, and the accuracy of Z_{eff} is found to be better than 1% (see Supporting Information S1).

We first chose Sn as a controlled sample to test ZEM's capability to detect hydrogen. Figure 2a, b shows a Sn microball's SEM and corresponding A_{th} image. Unlike the SEM image, where brightness and contrast can be arbitrarily adjusted by the user, the brightness and contrast of A_{th} images are fixed, allowing an absolute color bar of absorbance for each ZEM image. This advantage of ZEM thus enables quantitative Z analysis.

Because the Z of Sn is $Z_{\text{Sn}} = 50$, the Z_{eff} of SnH_x would be $Z_{\text{SnH}} = (50 + x)/(1 + x) < Z_{\text{Sn}}$. From Figure 1c, the hydrogen absorption would reduce Z_{eff}, and correspondingly, displays an enhanced A_{th}. On the other hand, because it has been known that surface morphology, such as tilted facets, edges, or voids, would also alter the signals of ZEM,[23] we employ a normalized quantity $(A_{\text{th}}(SnH_x) - A_{\text{th}}(Sn))/A_{\text{th}}(Sn)$ to eliminate their effects and to highlight the Z_{eff} variations (see Supporting Information S2). Figure 2c displays the variations of $(A_{\text{th}}(SnH_x) - A_{\text{th}}(Sn))/A_{\text{th}}(Sn)$ of the Sn microball. Note that only the crack region displays hydrogen absorption. Interestingly, Figure 2d shows that the amount of hydrogen in the crack decreases after 30 min, indicating desorption of hydrogen occurs in the SEM chamber (vacuum pressure $<10^{-5}$ mbar). Because Sn is not a hydrogen storage material and cracks are known to physically absorb hydrogen stronger than other regions, the result confirms ZEM's capability in detecting hydrogen in materials.

Next, we choose palladium (Pd) as a representative hydrogen storage sample. Pd has been a prototypical metal-hydride system in virtually every aspect of the envisioned hydrogen economy, including hydrogen purification, storage, detection, and fuel cells.[28] Pd exhibits fast dissociation kinetics of molecular hydrogen at its surfaces, showing high bulk diffusivity of atomic hydrogen at room temperature and atmospheric pressure. Thus, Pd has been used as a catalyst to facilitate the uptake and dissociation of hydrogen in other metal hydrides, reducing their hydrogenation time.[28] The bulk PdH_x phase diagram exhibits a miscibility gap below 290 °C between a diluted α phase with $x < 0.017$ and a concentrated β phase with $x > 0.6$ at room temperature. On the other hand, because of the accompanied lattice distortion during hydrogenation processes, the elastic energy barrier of Pd is size- and shape-dependent, leading to distinct thermodynamic phenomena at the nanoscale.[29−32] Unfortunately, our understanding of hydrogen absorption and desorption in Pd remains incomplete, primarily because vacancies and other defects are nearly undetectable using conventional nanoscale characterization techniques. Moreover, the relationship between defect formation and repeated hydrogen charging/discharging pro-

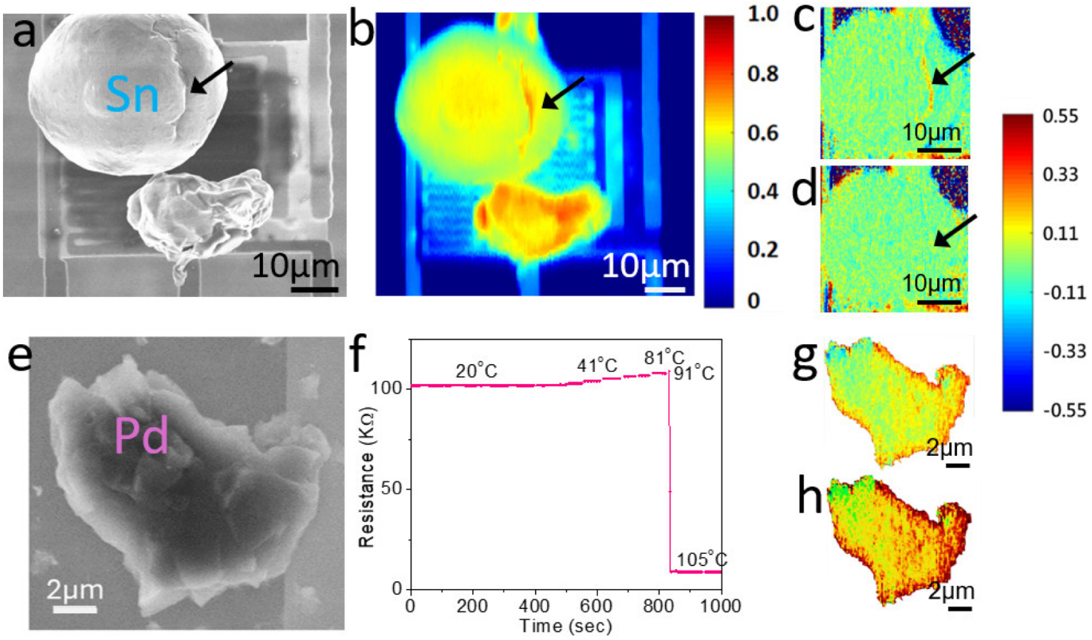

Figure 2. Quantifying hydrogen storage using ZEM. (a and b) An SEM image and the corresponding ZEM image of a Sn microball. Note that there is a crack (indicated by an arrow) in the microball. (c) Mapping of ($A_{th}(SnH_x) - A_{th}(Sn))/A_{th}(Sn)$ after charging hydrogen and (d) after putting the sample in the SEM chamber 30 min later. Notice the disappearance of hydrogen absorption in the crack (indicated by an arrow). (e) An SEM image of a Pd micrograin. (f) Time-dependent electrical resistance measurement of a PdH_x micrograin. The temperature of the PdH_x micrograin is gradually raised until hydrogen desorption occurs at 91 °C. (g) Mapping of $(A_{th}(PdH_x) - A_{th}(Pd))/A_{th}(Pd)$ after charging hydrogen. Here, the average hydrogen content $x = 10\%$. The color bar is for (c, d, g). (h) Enhanced contrast of (g) to show the correlation between x and the grain boundaries shown in (e).

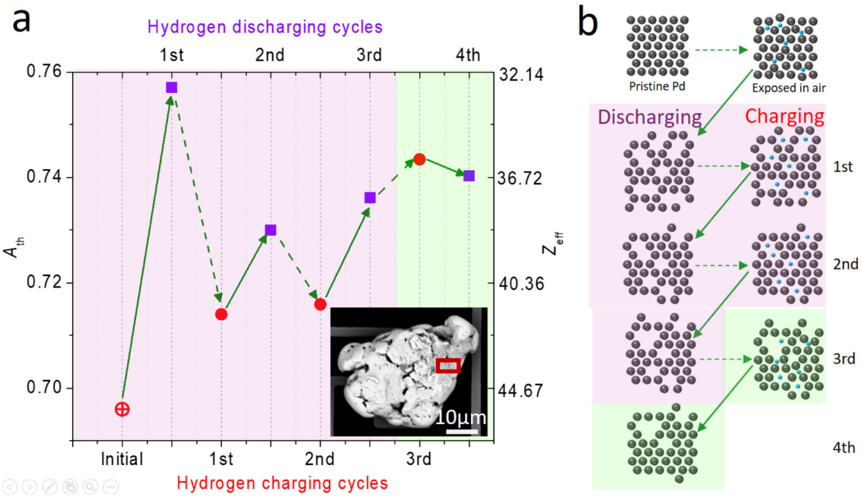

Figure 3. Evolution of A_{th} and Z_{eff} for multiple hydrogen charging−discharging cycles. (a) The evolution of A_{th} (left axis) and Z_{eff} (right axis) for a Pd micrograin undergoing three hydrogen charging−discharging cycles. The discharged (solid arrows) and charged (dashed arrows) processes would result in Pd (purple squares) or PdH_x (red circles). The insets show the SEM image of the Pd micrograin. The A_{th} of a pristine Pd, determined by CASINO simulation ($(A_{th}(Pd))_0 = 0.696$), is denoted as the open-crossed circle. The measurement uncertainties of A_{th} is estimated to be ±1%. (b) Schematic illustrations of the hydrogen uptake and defect formation processes during the charging−discharging cycles. Here, Pd and hydrogen atoms are denoted as dark gray and blue circles, respectively. Two distinct phenomena, respectively showing $A_{th}(PdH)_m < A_{th}(Pd)_m$ ($m = 1, 2, 3$) and $A_{th}(PdH)_3 > A_{th}(Pd)_4$ are denoted by the shaded purple and green regions, respectively. The former suggests that most hydrogens fill the defects after charging (leading to an increase of Z_{eff}) while the latter indicates hydrogens react with Pd (leading to a decreased Z_{eff}). Defects healing after discharging is observed in both cases.

cesses is unknown. These challenges make Pd an ideal candidate for ZEM characterization, offering a promising approach to gaining deeper insights into nanoscale hydrogenation dynamics.

Similar to the Sn microball, we repeated the experiment on a Pd micrograin, whose SEM image is shown in Figure 2e. Because Pd is a metal, whereas PdH_x is a semiconductor, an independent resistance measurement of a Pd grain can be carried out simultaneously to monitor its hydrogen uptake. Figure 2f shows that the high resistance state can be kept for a long time in a vacuum chamber until the sample is heated beyond 91 °C to discharge the hydrogen. Figure 2g displays

https://doi.org/10.1021/acsnano.4c16841
ACS Nano 2025, 19, 10070−10077

the mapping of $(A_{\mathrm{th}}(\mathrm{PdH}_x) - A_{\mathrm{th}}(\mathrm{Pd})_0)/A_{\mathrm{th}}(\mathrm{Pd})_0$ (where $A_{\mathrm{th}}(\mathrm{Pd})_0$ is the of a pristine Pd, in which no hydrogen absorption has occurred) of a Pd micrograin. The relation of $(A_{\mathrm{th}}(\mathrm{PdH}_x) - A_{\mathrm{th}}(\mathrm{Pd})_0)/A_{\mathrm{th}}(\mathrm{Pd})_0$ vs x established by ZEM enables us to obtain x's distribution (see Supporting Information S3). Although high x appeared at the edges of Figure 2g are probably due to artifacts of imaging processing (originating from scanning drift and the lattice expansion of PdH_x that make precisely locating the edges of the micrograin difficult,[33] averaging the whole area of the micrograin gives $x = 10\%$. Curiously, x is inhomogeneously distributed; some regions appear to absorb hydrogen with considerably higher $x \sim 36\%$ while others exhibit $x \sim 0\%$. After enhancing the contrast shown in Figure 2h, we observe correlations between the x and the grain boundaries. Because of a significant volume fraction of grain interfaces, the hydrogen solubility in the nanocrystalline Pd film is much higher than in a conventional bulk Pd.[29,32,34−36] Besides, surface effects, defects, and internal stresses at the grain boundaries may influence hydrogen solubility as well,[6,29,32,36] resulting in the observed $x = 36\%$. The determination of x and its correlation with grain boundaries thus demonstrate ZEM's capability to detect hydrogen at the nanoscale.

The Evolution of Hydrogens and Defects via Cyclic Charging−Discharging. Because $A_{\mathrm{th}}(\mathrm{Pd})_0$ is not always experimentally available, we choose $A_{\mathrm{th}}(\mathrm{Pd})_0 = 0.696$ obtained from CASINO simulation in the following works. Experimentally, we will discharge a Pd micrograin first before undergoing multiple hydrogen charging−discharging cycles. The A_{th}'s from a selected flat region of the Pd micrograin is used to represent the Z variations. A flat region will enable its absolute A_{th} to be determined without unwanted perturbations from tilted facets, edges, cracks, or other surface morphological effects.[23]

Our initial observation in Figure 3a reveals that the A_{th} of the first discharged Pd ($A_{\mathrm{th}}(\mathrm{Pd})_1 = 0.757$) is much higher than that of $A_{\mathrm{th}}(\mathrm{Pd})_0$, which is equivalent to a reduction of Z_{eff} from 46 to 32.6. To explain the result, we note that superabundant vacancies,[37−39] vacancy-ordered phases,[38,40,41] and reduction of vacancy formation enthalpy after hydrogenation[42] have been found in bulk Pd. Because monovacancies ($Z_{\mathrm{Vac}} = 0$) and other forms of defects would enhance A_{th} and, correspondingly, reduce Z_{eff} of Pd (see Supporting Information S4), the reduction of Z_{eff} beyond its initial value $Z_{\mathrm{Pd}} = 46$ after the first discharging shown in Figure 3a suggests the presence of defects.

From $Z_{\mathrm{PdH}} = (46 + x)/(1 + x)$ for PdH_x and $Z_{\mathrm{PdVac}} = 46/(1 + \nu_{\mathrm{eff}})$ for Pd containing ν_{eff} defects in a unit cell (assuming $Z_{\mathrm{Vac}} = 0$ for a monovacancy and other forms of defects, here ν_{eff} is the effective defect density), we find that while x varies at around 11% for the first two cycles in Figure 3a, ν_{eff} reaches the highest value of 40% at the first cycle and reduces to $\nu_{\mathrm{eff}} = 25\%$ at the third cycle. The estimated ν_{eff} is higher than those reported in the literature because it contains contributions from other forms of defects (including voids, see Supporting Information S4). Based on the known result that hydrogens in PdH_x randomly occupy the lattice interstices,[43] we illustrate the lattice model of the initially charged PdH_x in the first row of Figure 3b and the formation of defects in the second row of Figure 3b for the discharged Pd model.

When repeating hydrogen charging, Figure 3a shows $A_{\mathrm{th}}(\mathrm{PdH})_{\mathrm{m}} < A_{\mathrm{th}}(\mathrm{Pd})_{\mathrm{m}}$ ($m = 1, 2, 3$) and oscillations of A_{th} are observed. Naively, if the charged hydrogens continue to fill the lattice interstices and become PdH_x, the Z_{eff} should have decreased and an opposite effect (i.e., $A_{\mathrm{th}}(\mathrm{PdH})_{\mathrm{m}} > A_{\mathrm{th}}(\mathrm{Pd})_{\mathrm{m}}$) should have been observed. To explain the data, hydrogens ($Z_{\mathrm{H}} = 1$) must fill the defects ($Z_{\mathrm{Vac}} = 0$) so as to increase the Z_{eff} and to be consistent with the observation of $A_{\mathrm{th}}(\mathrm{PdH})_{\mathrm{m}} < A_{\mathrm{th}}(\mathrm{Pd})_{\mathrm{m}}$ ($m = 1, 2, 3$). The corresponding lattice models are illustrated in the second to the fourth rows of Figure 3b.

Curiously, we observe $A_{\mathrm{th}}(\mathrm{Pd})_{\mathrm{first}} > A_{\mathrm{th}}(\mathrm{Pd})_{2\ \mathrm{rd}} \sim A_{\mathrm{th}}(\mathrm{Pd})_{\mathrm{third}}$ in Figure 3a, indicating that ν_{eff} is reduced after the second discharging. The unusual phenomenon has been suggested by theoretical calculations that voids in Pd are thermodynamically unstable due to the loss of configurational entropy upon coalescing of monovacancy complexes.[44] In fact, stable voids in Pd are attributed to other factors, such as strain induced by hydrogen dissolution or hydrogen-enhanced local plasticity.[44,45] Because the time scale for conducting our experiment suggests that the observed ν_{eff} in the Pd micrograin remains relatively stable at least for days, Figure 3a indicates that ν_{eff} would change only when the Pd undergoes cyclic charging−discharging processes. During the hydrogen charging process, lattice strain would increase, facilitating the decomposition of voids into monovacancies via defect migration.[46] Thus, $A_{\mathrm{th}}(\mathrm{Pd})_{\mathrm{first}} > A_{\mathrm{th}}(\mathrm{Pd})_{2\ \mathrm{rd}} \sim A_{\mathrm{th}}(\mathrm{Pd})_{\mathrm{third}}$ suggests a healing process of voids, as illustrated in Figure 3b.

The healing process of voids may also explain why the ratio of vacancy to hydrogen concentration is high ($\nu_{\mathrm{eff}}/x = 3.6$) at the beginning and decreases to $\nu_{\mathrm{eff}}/x = 0.85$ after the third cycle. It has been suggested that up to six hydrogen atoms can be captured by a monovacancy,[47,48] whereas the number of hydrogens captured by a void should be less due to the reduced surface-to-volume ratio. Because the initial ν_{eff} contains a larger contribution of voids that tend to overestimate ν_{eff} by a factor of 3.5 (see Supporting Information S4), the reduction of ν_{eff}/x also suggests the decomposition of voids into monovacancies during the cyclic hydrogen charging−discharging processes.

We notice that the oscillation amplitude $[A_{\mathrm{th}}(\mathrm{Pd})_{\mathrm{m}} - A_{\mathrm{th}}(\mathrm{PdH})_{\mathrm{m}}$ ($m = 1, 2, 3$)] gradually decreases for increasing m and ν_{eff} becomes more for $m > 2$. After the third cycle, an opposite effect, $A_{\mathrm{th}}(\mathrm{PdH})_3 > A_{\mathrm{th}}(\mathrm{Pd})_4$, is observed. The result indicates that hydrogens no longer fill the defects, but they react with Pd instead. Currently, it is not known whether the Pd micrograin gradually loses its capability to uptake hydrogen or there is a balance between the two opposite effects (i.e., $A_{\mathrm{th}}(\mathrm{PdH})_{\mathrm{m}} < A_{\mathrm{th}}(\mathrm{Pd})_{\mathrm{m}}$ and $A_{\mathrm{th}}(\mathrm{PdH})_{\mathrm{m}} > A_{\mathrm{th}}(\mathrm{Pd})_{\mathrm{m}}$).

Because similar phenomena, including a jump of A_{th} in the first discharging and oscillations of A_{th}'s at the later cycles, are observed in Region II and in another Pd micrograin (see Supporting Information S5 and S6), they could suggest a universal defect formation and healing phenomenon.

Compared with other techniques, the differential thermal expansion method relies on X-ray or TEM diffraction to determine the lattice contraction, which is sensitive to monovancancies only. PAS depends on the lifetime measurements of positrons, and the estimation of defect concentrations relies on the parameters of the trapping model, which has been known to be inadequate for materials with superabundant vacancies.[49,50] Thus, the excess ν_{eff} observed by ZEM indicates that previous characterization tools could have missed voids, cracks, and cliffs.

Because the existing nanoscale hydrogen characterization tools, such as SIMS or APT, are constrained by their destructive detection methods, it is impossible for them to

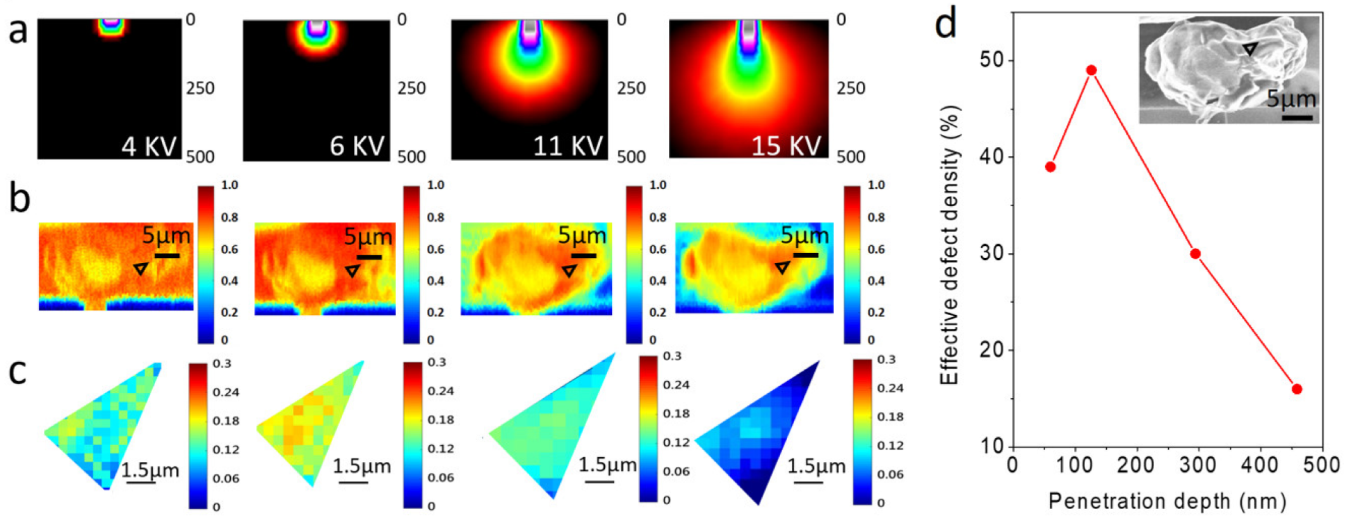

Figure 4. Depth profile of the effective defect density. (a) Simulated electron energy distribution under different V_{acc}'s (b) ZEM images of a Pd micrograin for different V_{acc}'s. (c) Mapping of $(A_{th}(PdH_x) - A_{th}(Pd))/A_{th}(Pd)$ on the flat region (denoted by the black triangles in (b)) of the Pd micrograin. (d) Effective defect density vs penetration depth of the flat region. The inset shows the SEM image of the Pd micrograin. The selected flat region for analysis is denoted as the black triangle. The ν_{eff}'s depth profile can be associated with the hydrogen uptake, hydrogen diffusion, defect creation, and defect healing processes in Pd.

reveal the cyclic charging−discharging process shown in Figure 3a. Thus, the unusual behavior shown in Figure 3a has never been reported to our knowledge.

The Depth Profile of Defect Density. Because varying the acceleration voltage (V_{acc}) of an electron beam is known to change the penetration depth (d) in a material,[51] ZEM can profile the defect density at different depths (see Supporting Information S7). Figure 4a shows the simulated interacting profiles of an electron beam accelerated at different V_{acc}'s and the associated d in Pd. We can see that increasing V_{acc} from 4 kV to 15 kV would increase the penetration depth from 60 to 458 nm, allowing us to probe deeper A_{th}'s beneath the surface. Figures 4b,c show the ZEM images at different V_{acc}'s and the corresponding flat region selected for Z analysis. Interestingly, we find ν_{eff} increases from 39% at d = 60 nm to 49% at d = 126 nm and decreases to 16% at d = 458 nm, as shown in Figure 4d. As mentioned above, the ν_{eff}'s observed here may also contain contributions of monovacancies, voids, cracks, and other defects. Because hydrogen is known to reduce the defect formation energy and facilitate the motion of dislocations,[52−54] the observed vacancy depth profile qualitatively agrees with the picture that hydrogen diffuses from the surface to the interior of Pd, creates various forms of defects, and the healing of the voids may further alter the distribution of ν_{eff} in the depth profile.

The Causality between Hydrogen Storage and Defect Formation. The relation between hydrogen storage and defect density has been established in bulk Pd, Nb, Ni, Co, and Fe,[55] in which the defect density is measured after a hydrogen charging−discharging cycle is applied. However, the lack of time-sequential analysis and the poor spatial resolution in previous works have prohibited the establishment of causality between hydrogen storage and defect formation. Here, we are particularly curious about the question: After the first cycle, do hydrogens continue to create defects in Pd, or do the preexisting defects become the primary sites attracting hydrogen in subsequent cycles?

To answer the former question, we have applied pixel-by-pixel correlation analysis for ZEM images of hydrogen content and defect density at the mth cycle (m = 2, 3), in which hydrogen charging occurs first and discharging happens later. Interestingly, Figure 5 shows that the correlation is strong (correlation coefficient = 0.4−0.64) and agrees with previous results observed in bulk metal hydrides.

To answer the latter question, we investigate the defect density at the mth cycle and the hydrogen content at the (m + 1)th cycle, in which the discharging occurs earlier than charging. Figure 5 shows a weaker correlation (correlation coefficient = 0.09−0.18), indicating that a significant number

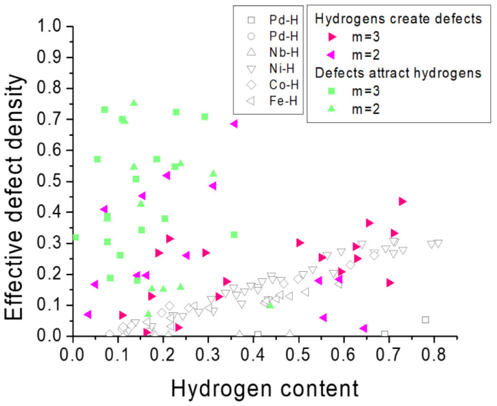

Figure 5. Causality between hydrogen storage content and the effective defect density. To investigate the causality, the data for "hydrogen creates defects" are obtained from the mth charging and discharging cycle in Figure 3, and the correlation coefficient = 0.4−0.64 is found. On the other hand, the data for "defects attract hydrogens" are obtained from the mth discharging cycle and the (m + 1)th charging cycle in Figure 3, and the correlation coefficient = 0.09−0.18 is obtained. Data established from bulk materials (open symbols) are also shown for comparison.[55] Our result suggests that hydrogenation creates defects, but defects do not necessarily attract hydrogens in Pd.

of defects exist but cannot attract the same amount of hydrogens. Note that the result does not contradict the model shown in Figure 3b, in which we find that some, but not all, defects are filled with hydrogens.

The distinct correlations establish the causality that hydrogenation creates defects, but defects do not necessarily attract hydrogens in Pd. At first glance, this might imply that ν_{eff} would continually increase with successive hydrogen charging−discharging cycles; however, this is certainly not the case. Thus, one possibility is the defect healing effect that decreases ν_{eff}. Another possibility is the correlation of hydrogen-creating-defects may become weaker for the $(m > 4)^{\mathrm{th}}$ cycles. Both of them have been observed in Figure 3.

CONCLUSION

Combining the new results provided by the ZEM, we now have a more complete understanding of hydrogen uptake and defect formation processes in Pd. Hydrogens enter Pd's surface and create various forms of defects. While the average hydrogen uptake in a PdH_x micrograin is $x \sim 10\%$, its distribution is highly inhomogeneous, reaching more than $x = 36\%$ at grain boundaries or defects. Hydrogens' diffusion into Pd's interior also generates a large defect density gradient, reaching $\nu_{\mathrm{eff}} = 49\%$ at 126 nm beneath the surface and $\nu_{\mathrm{eff}} = 16\%$ in the interior of Pd. While some of the defects may attract hydrogens during charging, voids may decompose into monovacancies due to their thermodynamic instability. Defects are considered the precursor of hydrogen embrittlement;[3,4,52−54,56,57] however, very few existing tools can characterize them at the nanoscale. These results demonstrate ZEM's potential for material characterizations, especially for unraveling the role of hydrogens and defects in the science of catalysis and sustainable energy.

METHODS

Materials. Palladium (Pd) fine powders with 99.995% purity were obtained from Sigma-Aldrich. The powders were dispersed in alcohol and deposited onto a ZEM measurement platform. Hydrogen discharging was performed within the SEM chamber by applying a high Joule heating current to the ZEM platform, raising its temperature above 120 °C for 30 min. For hydrogen charging, the Pd sample was exposed to 99.999% pure hydrogen at a pressure of 1.5 bar for 1 h in a custom-built chamber. Following this process, the sample was rapidly transferred to the SEM chamber for analysis.

Measurements. ZEM measurements were performed using a Zeiss Auriga SEM. A LabView program controlled the raster scanning of a focused electron beam across the sample. A Keithley 224 current source supplied DC currents, while voltage responses from the ZEM platform were recorded using a Wheatstone bridge setup with an HP/Agilent 34970A data acquisition system. The ZEM images of discharged Pd micrograin were scanned twice to obtain the normalized variation of A_{th}, which minimizes the unwanted effects of structural perturbations.

Simulations. The simulations were performed using the CASINO Monte Carlo program (Version 3.3.0.4) with the MONSEL Defaults model. This model integrates the Browning approach for calculating the Mott elastic scattering cross-section and employs the Joy and Luo model, further modified by Lowney, to compute inelastic scattering energy loss (dE/dS). In each simulation, 100,000 electrons were input with varying electron beam diameters and acceleration voltages ($V_{\mathrm{acc}} = 1{-}20$ kV). This setup allowed for the determination of interaction volume, reflectance (R), transmittance (T), absorbance (A), the effective defect density (ν_{eff}), and the penetration depth (d) based on the specified parameters. Please see Supporting Information for more details.

ASSOCIATED CONTENT

Supporting Information

The Supporting Information is available free of charge at https://pubs.acs.org/doi/10.1021/acsnano.4c16841.

> Experimental procedures and the accuracy and precision of A_{th} measurements; image processing; the relation between A_{th}, Z_{eff}, and hydrogen content (x); Monte Carlo simulation of the absorbance of voids; the evolution of hydrogens and defects in Region II; the evolution of hydrogens and defects of another Pd micrograin; and the electron beam's penetration depth (d) vs V_{acc} (PDF)

AUTHOR INFORMATION

Corresponding Author

Chih-Wei Chang − *Center for Condensed Matter Sciences, National Taiwan University, Taipei 10617, Taiwan; Center of Atomic Initiative for New Materials (AI-MAT), National Taiwan University, Taipei 10617, Taiwan;* orcid.org/0000-0003-0956-3179; Email: cwchang137@ntu.edu.tw

Authors

Yu-Cheng Chiu − *Center for Condensed Matter Sciences, National Taiwan University, Taipei 10617, Taiwan; Department of Mechanical Engineering, National Cheng Kung University, Tainan 70101, Taiwan*

Bo-Yi Chen − *Center for Condensed Matter Sciences, National Taiwan University, Taipei 10617, Taiwan*

Chin-Chia Hsu − *Center for Condensed Matter Sciences, National Taiwan University, Taipei 10617, Taiwan; Department of Mechanical Engineering, National Cheng Kung University, Tainan 70101, Taiwan*

Chia-Wei Tsai − *Center for Condensed Matter Sciences, National Taiwan University, Taipei 10617, Taiwan; Department of Mechanical Engineering, National Cheng Kung University, Tainan 70101, Taiwan*

Shih-Ming Wang − *Center for Condensed Matter Sciences, National Taiwan University, Taipei 10617, Taiwan; Department of Mechanical Engineering, National Cheng Kung University, Tainan 70101, Taiwan*

I-Ling Chang − *Department of Mechanical Engineering, National Cheng Kung University, Tainan 70101, Taiwan*

Complete contact information is available at: https://pubs.acs.org/10.1021/acsnano.4c16841

Notes

The authors declare no competing financial interest.

ACKNOWLEDGMENTS

This work is supported by the Ministry of Science and Technology of Taiwan (MOST 111-2112-M-002-043-MY3 and 110-2119-M-002-010-MBK) and the Center of Atomic Initiative for New Materials, National Taiwan University, from the Featured Areas Research Center Program within the framework of the Higher Education Sprout Project by the Ministry of Education in Taiwan (108L9008).

REFERENCES

(1) Pudukudy, M.; Yaakob, Z.; Mohammad, M.; Narayanan, B.; Sopian, K. Renewable hydrogen economy in Asia - Opportunities and challenges: An overview. *Renewable Sustainable Energy Rev.* **2014**, *30*, 743−757.

(2) Moliner, R.; Lázaro, M. J.; Suelves, I. Analysis of the strategies for bridging the gap towards the Hydrogen Economy. *Int. J. Hydrogen Energy* **2016**, *41*, 19500−19508.

(3) Zhong, W.; Cai, Y.; Tomanek, D. Computer-Simulation of Hydrogen Embrittlement in Metals. *Nature* **1993**, *362*, 435−437.

(4) Song, J.; Curtin, W. A. Atomic mechanism and prediction of hydrogen embrittlement in iron. *Nat. Mater.* **2013**, *12*, 145−151.

(5) Chen, Y. S.; Haley, D.; Gerstl, S. S. A.; London, A. J.; Sweeney, F.; Wepf, R. A.; Rainforth, W. M.; Bagot, P. A. J.; Moody, M. P. Direct observation of individual hydrogen atoms at trapping sites in a ferritic steel. *Science* **2017**, *355*, 1196−1199.

(6) Chen, Y.-S.; Lu, H.; Liang, J.; Rosenthal, A.; Liu, H.; Sneddon, G.; McCarroll, I.; Zhao, Z.; Li, W.; Guo, A.; Cairney, J. M. Observation of hydrogen trapping at dislocations, grain boundaries, and precipitates. *Science* **2020**, *367* (6474), 171−175.

(7) Prins, R. Hydrogen Spillover. Facts and Fiction. *Chem. Rev.* **2012**, *112*, 2714−2738.

(8) Karim, W.; Spreafico, C.; Kleibert, A.; Gobrecht, J.; VandeVondele, J.; Ekinci, Y.; van Bokhoven, J. A. Catalyst support effects on hydrogen spillover. *Nature* **2017**, *541* (7635), 68−71.

(9) Jiang, L.; Liu, K.; Hung, S.-F.; Zhou, L. Y.; Qin, R.; Zhang, Q.; Liu, P.; Gu, L.; Chen, H.; Fu, G.; Zheng, N. Facet engineering accelerates spillover hydrogenation on highly diluted metal nanocatalysts. *Nat. Nanotechnol.* **2020**, *15* (10), 848−853.

(10) Liu, Q.; Xu, W.; Huang, H.; Shou, H.; Low, J.; Dai, Y.; Gong, W.; Li, Y.; Duan, D.; Zhang, W.; Jiang, Y.; et al. Spectroscopic visualization of reversible hydrogen spillover between palladium and metal−organic frameworks toward catalytic semihydrogenation. *Nat. Commun.* **2024**, *15* (1), 2562.

(11) Lin, H. J.; Li, H. W.; Shao, H. Y.; Lu, Y. S.; Asano, K. In situ measurement technologies on solid-state hydrogen storage materials: a review. *Mater. Today Energy* **2020**, *17*, 100463.

(12) Sun, C.; Wang, C. X.; Ha, T.; Lee, J.; Shim, J. H.; Kim, Y. A brief review of characterization techniques with different length scales for hydrogen storage materials. *Nano Energy* **2023**, *113*, 108554.

(13) Wei, T. Y.; Lim, K. L.; Tseng, Y. S.; Chan, S. L. I. A review on the characterization of hydrogen in hydrogen storage materials. *Renewable Sustainable Energy Rev.* **2017**, *79*, 1122−1133.

(14) Kelly, T. F.; Miller, M. K. Invited review article: Atom probe tomography. *Rev. Sci. Instrum.* **2007**, *78* (3), 031101.

(15) Rinaldi, R.; Llovet, X. Electron Probe Microanalysis: A Review of the Past, Present, and Future. *Microsc. Microanal.* **2015**, *21*, 1053−1069.

(16) Llovet, X.; Moy, A.; Pinard, P. T.; Fournelle, J. H. Electron probe microanalysis: A review of recent developments and applications in materials science and engineering. *Prog. Mater. Sci.* **2021**, *116*, 100673.

(17) Kwapisz, R.; Cone, R. L.; Thiel, C. W. Quantifying antisite defect concentrations in yttrium aluminum garnet by high-precision density analysis. *J. Lumin.* **2022**, *252*, 119408.

(18) Simmons, R. O.; Balluffi, R. W. Measurements of equilibrium vacancy concentrations in aluminum. *Phys. Rev.* **1960**, *117*, 52−61.

(19) Mills, S. H.; Zeltmann, S. E.; Ercius, P.; Kohnert, A. A.; Uberuaga, B. P.; Minor, A. M. Nanoscale mapping of point defect concentrations with 4D-STEM. *Acta Mater.* **2023**, *246*, 118721.

(20) Tuomisto, F.; Makkonen, I. Defect identification in semiconductors with positron annihilation: Experiment and theory. *Rev. Mod. Phys.* **2013**, *85*, 1583−1631.

(21) Gigl, T.; Beddrich, L.; Dickmann, M.; Rienacker, B.; Thalmayr, M.; Vohburger, S.; Hugenschmidt, C. Defect imaging and detection of precipitates using a new scanning positron microbeam. *New J. Phys.* **2017**, *19*, 123007.

(22) Yuan, P. Y.; Wu, J. Y.; Ogletree, D. F.; Urban, J. J.; Dames, C.; Ma, Y. B. Adapting the Electron Beam from SEM as a Quantitative Heating Source for Nanoscale Thermal Metrology. *Nano Lett.* **2020**, *20*, 3019−3029.

(23) Lin, C. C.; Wang, S. M.; Chen, B. Y.; Chi, C. H.; Chang, I. L.; Chang, C. W. Scanning Electron Thermal Absorbance Microscopy for Light Element Detection and Atomic Number Analysis. *Nano Lett.* **2022**, *22*, 2667−2673.

(24) Wang, S. M.; Chiu, Y. C.; Wu, Y. H.; Chen, B. Y.; Chang, I. L.; Chang, C. W. Standardization and quantification of backscattered electron imaging in scanning electron microscopy. *Ultramicroscopy* **2024**, *262*, 113982.

(25) Hovington, P.; Drouin, D.; Gauvin, R. CASINO: A new Monte Carlo code in C language for electron beam interaction.1. Description of the program. *Scanning* **1997**, *19*, 1−14.

(26) Hovington, P.; Drouin, D.; Gauvin, R.; Joy, D. C.; Evans, N. CASINO: A new Monte Carlo code in C language for electron beam interactions.3. Stopping power at low energies. *Scanning* **1997**, *19*, 29−35.

(27) Drouin, D.; Hovington, P.; Gauvin, R. CASINO: A new Monte Carlo code in C language for electron beam interactions.2. Tabulated values of the Mott cross section. *Scanning* **1997**, *19*, 20−28.

(28) Adams, B. D.; Chen, A. C. The role of palladium in a hydrogen economy. *Mater. Today* **2011**, *14*, 282−289.

(29) Baldi, A.; Narayan, T. C.; Koh, A. L.; Dionne, J. A. In-situ detection of hydrogen-induced phase transitions in individual palladium nanocrystals. *Nat. Mater.* **2014**, *13*, 1143−1148.

(30) Bardhan, R.; Hedges, L. O.; Pint, C. L.; Javey, A.; Whitelam, S.; Urban, J. J. Uncovering the intrinsic size dependence of hydriding phase transformations in nanocrystals. *Nat. Mater.* **2013**, *12*, 905−912.

(31) Griessen, R.; Strohfeldt, N.; Giessen, H. Thermodynamics of the hybrid interaction of hydrogen with palladium nanoparticles. *Nat. Mater.* **2016**, *15*, 311−317.

(32) Syrenova, S.; Wadell, C.; Nugroho, F. A. A.; Gschneidtner, T. A.; Fernandez, Y. A. D.; Nalin, G.; Switlik, D.; Westerlund, F.; Antosiewicz, T. J.; Zhdanov, V. P.; Moth-Poulsen, K.; Langhammer, C. Hydride formation thermodynamics and hysteresis in individual Pd nanocrystals with different size and shape. *Nat. Mater.* **2015**, *14* (12), 1236−1244.

(33) Peisl, H., Lattice strains due to hydrogen in metals. In *In Hydrogen in Metals I: Basic Properties*; Springer: Berlin Heidelberg: Berlin, Heidelberg, 1978; pp. 53−74.

(34) Pundt, A.; Kirchheim, R. Hydrogen in metals: Microstructural aspects. *Annu. Rev. Mater. Res.* **2006**, *36*, 555−608.

(35) Cizek, J.; Prochazka, I.; Danis, S.; Melikhova, O.; Vlach, M.; Zaludova, N.; Brauer, G.; Anwand, W.; Mücklich, A.; Gemma, R.; Nikitin, E.; Kirchheim, R.; Pundt, A. Positron annihilation study of hydrogen trapping at open-volume defects: Comparison of nanocrystalline and epitaxial Nb thin films. *J. Alloys Compd.* **2007**, *446*, 484−488.

(36) Cízek, J.; Melikhova, O.; Vlcek, M.; Lukác, F.; Vlach, M.; Procházka, I.; Anwand, W.; Brauer, G.; Mücklich, A.; Wagner, S.; Uchida, H.; Pundt, A. Hydrogen-induced microstructural changes of Pd films. *Int. J. Hydrogen Energy* **2013**, *38*, 12115−12125.

(37) Fukai, Y.; Okuma, N. Evidence of Copious Vacancy Formation in Ni and Pd under a High Hydrogen Pressure. *Jpn. J. Appl. Phys.* **1993**, *32*, L1256−L1259.

(38) Fukai, Y.; Okuma, N. Formation of Superabundant Vacancies in Pd Hydride under High Hydrogen Pressures. *Phys. Rev. Lett.* **1994**, *73*, 1640−1643.

(39) Fukai, Y. Formation of superabundant vacancies in M-H alloys and some of its consequences: a review. *J. Alloys Compd.* **2003**, *356*, 263−269.

(40) dos Santos, D. S.; Miraglia, S.; Fruchart, D. A high pressure investigation of Pd and the Pd-H system. *J. Alloys Compd.* **1999**, *291*, L1−L5.

(41) Miraglia, S.; Fruchart, D.; Hlil, E. K.; Tavares, S. S. M.; Dos Santos, D. Investigation of the vacancy-ordered phases in the Pd-H system. *J. Alloys Compd.* **2001**, *317*, 77−82.

(42) Polfus, J. M.; Peters, T.; Bredesen, R.; Lovvik, O. M. Vacancy diffusion in palladium hydrides. *Phys. Chem. Chem. Phys.* **2021**, *23*, 13680−13686.

(43) McLennan, K. G.; Gray, E. M.; Dobson, J. F. Deuterium occupation of tetrahedral sites in palladium. *Phys. Rev. B* **2008**, *78*, 014104.

(44) Polfus, J. M.; Lovvik, O. M.; Bredesen, R.; Peters, T. Hydrogen induced vacancy clustering and void formation mechanisms at grain boundaries in palladium. *Acta Mater.* **2020**, *195*, 708−719.

(45) Al-Mufachi, N. A.; Rees, N. V.; Steinberger-Wilkens, R. Hydrogen selective membranes: A review of palladium-based dense metal membranes. *Renewable Sustainable Energy Rev.* **2015**, *47*, 540−551.

(46) Wagner, S.; Kramer, T.; Uchida, H.; Dobron, P.; Cizek, J.; Pundt, A. Mechanical stress and stress release channels in 10−350 nm palladium hydrogen thin films with different micro-structures. *Acta Mater.* **2016**, *114*, 116−125.

(47) Vekilova, O. Y.; Bazhanov, D. I.; Simak, S. I.; Abrikosov, I. A. First-principles study of vacancy-hydrogen interaction in Pd. *Phys. Rev. B* **2009**, *80*, 024101.

(48) Nazarov, R.; Hickel, T.; Neugebauer, J. Ab initio study of H-vacancy interactions in fcc metals: Implications for the formation of superabundant vacancies. *Phys. Rev. B* **2014**, *89*, 144108.

(49) Roddatis, V.; Bongers, M. D.; Vink, R.; Burlaka, V.; Cizek, J.; Pundt, A. Insights into Hydrogen Gas Environment-Promoted Nanostructural Changes in Stressed and Relaxed Palladium by Environmental Transmission Electron Microscopy and Variable-Energy Positron Annihilation Spectroscopy. *J. Phys. Chem. Lett.* **2018**, *9*, 5246−5253.

(50) Sakaki, K.; Yamada, T.; Mizuno, M.; Araki, H.; Shirai, Y. Hydrogen-induced vacancy generation phenomenon in pure Pd. *Mater. Trans.* **2002**, *43*, 2652−2655.

(51) Kanaya, K.; Okayama, S. Penetration and Energy-Loss Theory of Electrons in Solid Targets. *J. Phys. D: Appl. Phys.* **1972**, *5* (1), 43.

(52) Bhadeshia, H. K. D. H. Prevention of Hydrogen Embrittlement in Steels. *ISIJ Int.* **2016**, *56*, 24−36.

(53) Barnoush, A.; Vehoff, H. Recent developments in the study of hydrogen embrittlement: Hydrogen effect on dislocation nucleation. *Acta Mater.* **2010**, *58*, 5274−5285.

(54) Robertson, I. M.; Sofronis, P.; Nagao, A.; Martin, M. L.; Wang, S.; Gross, D. W.; Nygren, K. E. Hydrogen Embrittlement Understood. *Metall. Mater. Trans. A* **2015**, *46a*, 2323−2341.

(55) Fukai, Y.; Sugimoto, H. Formation mechanism of defect metal hydrides containing superabundant vacancies. *J. Phys.: Condens. Matter* **2007**, *19*, 436201.

(56) Iwamoto, M.; Fukai, Y. Superabundant vacancy formation in iron under high hydrogen pressures: Thermal desorption spectroscopy. *Mater. Trans., JIM* **1999**, *40*, 606−611.

(57) Cuitino, A. M.; Ortiz, M. Ductile fracture by vacancy condensation in FCC single crystals. *Acta Mater.* **1996**, *44*, 427−436.

Supporting Information

Quantitatively profiling the evolution of hydrogen storage and defect healing processes of palladium at the nanoscale

Yu-Cheng Chiu,[1,2] Bo-Yi Chen,[1] Chin-Chia Hsu,[1,2] Chia-Wei Tsai,[1,2] Shih-Ming Wang,[1,2] I-Ling Chang,[2] and Chih-Wei Chang[1,3*]

[1] Center for Condensed Matter Sciences, National Taiwan University, Taipei 10617, Taiwan

[2] Department of Mechanical Engineering, National Cheng Kung University, Tainan 70101, Taiwan

[3] Center of Atomic Initiative for New Materials (AI-MAT), National Taiwan University, Taipei, 10617, Taiwan

S1. Experimental procedures and the accuracy and precision of A_{th} measurements.

Palladium (Pd) fine powders with 99.995% purity were purchased from Sigma-Aldrich. They were dispersed in alcohol and then dropped on a ZEM measurement platform. The hydrogen discharging process was made in the SEM chamber by applying a large Joule heating current to our ZEM platform to increase its temperature beyond 120°C for 0.5 hours. The hydrogen charging of Pd was carried out at 1.5 bar, under 99.999% pure hydrogen pressure, for 1 hour in our homemade chamber. Then, the sample was quickly transferred to our SEM chamber.

Similar to our previous work[1], the ZEM measurements were conducted using Zeiss Auriga SEM. A LabView program was used for raster-scanning a focused electron beam on a sample, while a Keithley 224 current source was used for supplying DC currents, and an HP/Agilent 34970A was used to read the voltage responses from the ZEM platform using a Wheatstone bridge.

Given that our ZEM signals are always normalized to A_{th} of a 400 nm thick SiN_x film, the SiN_x film effectively serves as the reference standard for calibration. However, because of the non-stoichiometric SiN_x, further calibration is necessary to precisely determine its Z. Figure S1(a & b) shows a single-beam bolometer with a stoichiometric Si_3N_4 (Z=10) nanowire deposited at its center. The single-beam bolometer allows all relevant physical quantities to be precisely measured. Figure S1(c) shows A_{th}'s of regions randomly selected from a SiN_x film. The measurement uncertainty is less than 1% for each image. Because of the presence of edges or tilted facets that would reduce A_{th}, the strongest A_{th}'s are selected from Fig. S1(c) to represent the intrinsic A_{th} of the Si_3N_4 nanowire. The results are compared with those of SiN_x film, and we find that $A_{th}(Si_3N_4 \text{ nanowire})/A_{th}(SiN_x \text{ film})=1.0084$. From the CASINO simulation, we have

A=0.89 for Si_3N_4 (Z=10). Thus, it suggests that the low-stress SiN_x film is in fact Si-rich and exhibits Z=11.3 (x=0.63). In addition, because A_{th}/A=98% of the SiN_x film has been established in our previous work and by P. Y. Yuan *et al.*[1,2], the accuracy of (A_{th}-A)/A is estimated to be 2%. This calibration procedure enables more accurate determinations of Z for other materials.

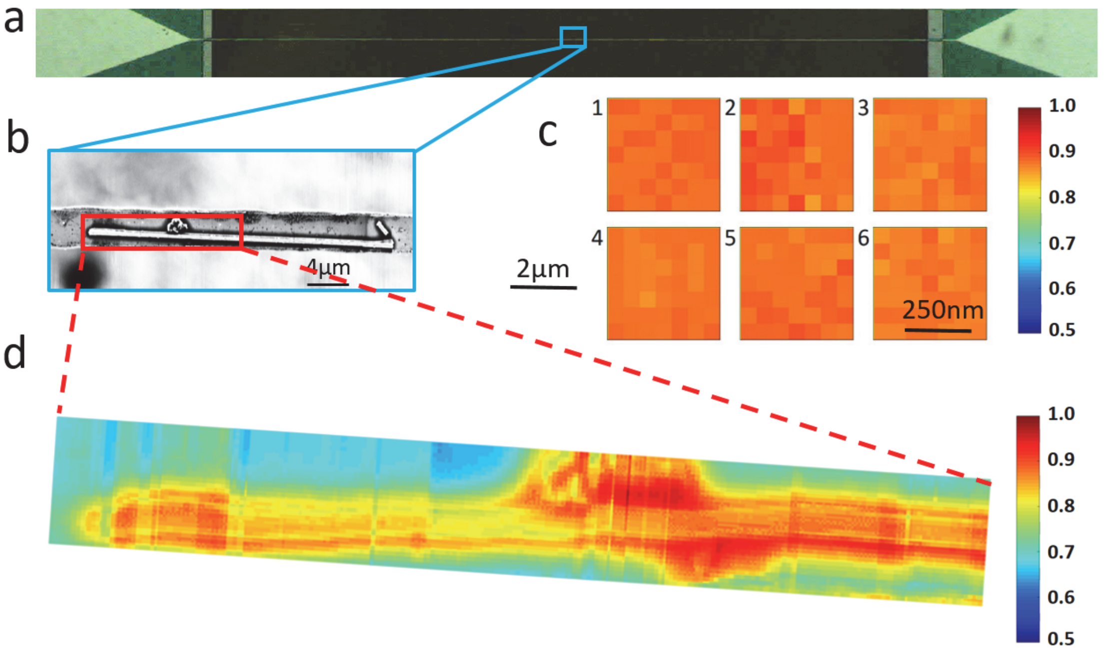

Fig. S1. Determining the accuracy and precision of A_{th} measurements. (a) An optical image of a 1450µm-long SiN_x beam with 50nm Pt film deposited on it. The setup is used for calibration of the A_{th} of a Si_3N_4 nanowire. (b) An enlarged SEM image of the center of a Si_3N_4 nanowire. (c) A_{th}'s of regions are randomly selected from a flat SiN_x film. For each 7×7 area, the measurement uncertainty is less than 1%. (d) A_{th} mapping of the Si_3N_4 nanowire. Its signals are compared with those of SiN_x film. We find A_{th}(Si_3N_4 nanowire)/A_{th}(SiN_x film)=1.0084.

We have also investigated the robustness of A_{th} measurements for prolonged scanning. As shown in Fig. S2(a), repeated and prolonged SEM scanning under low V_{acc} is known to cause hydrocarbon deposition on a sample. As displayed in Fig. S2(b), we have found that the effect is not pronounced for the A_{th} measurement of the Ag nanowire, Pt film, and SiN_x membrane shown in Fig. S2(a) when operating V_{acc} = 5KV for 4 hours (which is about the accumulated scanning time we conducted for the Pd micrograin undergoing multiple hydrogen charging-discharging cycles). From Fig. S2(b), the largest variation of A_{th} is found in the Ag nanowire, whose monotonic 5% increase can be attributed to the hydrocarbon deposition. On the other hand, A_{th}'s of the Pt film and the SiN_x membrane show ~1.7% variations that are much smaller than what we observe in Fig. 3 of the main text.

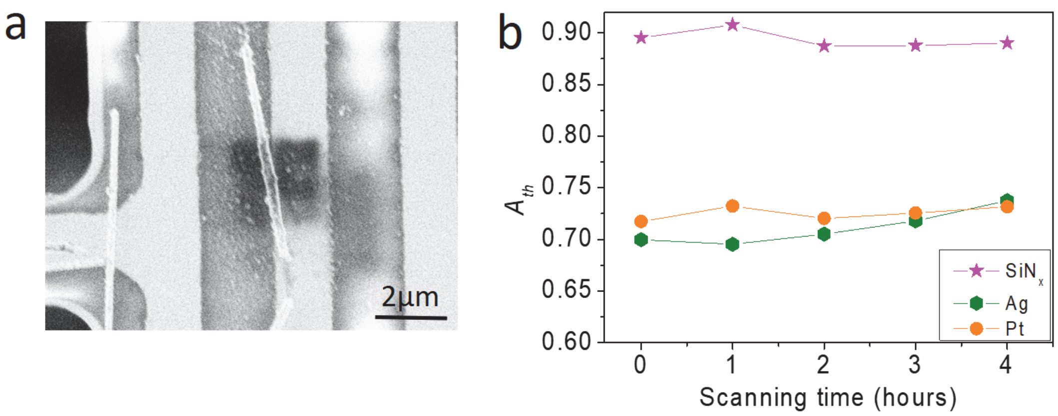

Fig. S2. Effects of prolonged A_{th} measurements. (a) SEM image of an area (the center dark square) after prolonged A_{th} measurements. (b) The corresponding A_{th} variations of the Ag nanowire, the Pt film, and the SiN_x membrane shown in (a).

S2. Image processing

The processes of obtaining the normalized variation of A_{th} images are shown in Fig. S3. Here the ZEM images of discharged Pd micrograin are scanned twice [respectively labelled as Pd(1) and Pd(2)], and the image of [Pd(2)−Pd(1)]/Pd(1) is obtained to highlight the relative A_{th} variations.

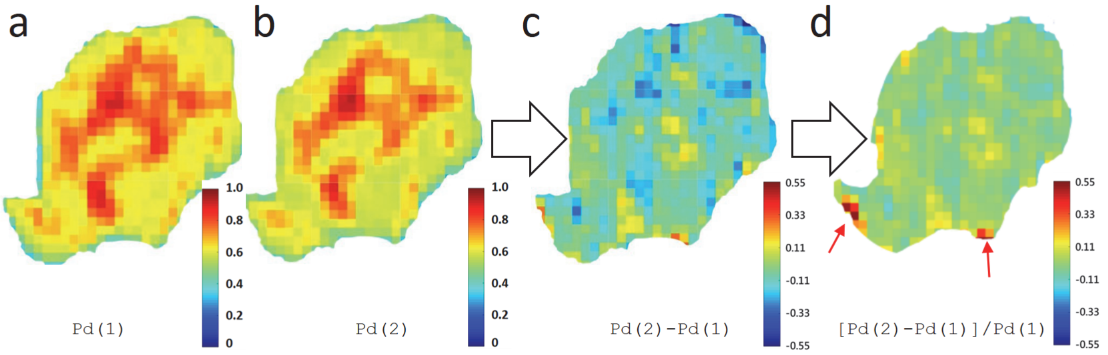

Fig. S3. Image processing procedures. (a & b) ZEM images of a Pd micrograin being scanned twice, whose A_{th} images are labelled as Pd(1) and Pd(2), respectively. Here the crack regions are displayed as red structures. (c) The image of Pd(2)−Pd(1). (d) The image of [Pd(2)−Pd(1)]/Pd(1). Note that the crack regions are almost invisible here. Due to the uncertainties in locating the edges, the image artifacts that appear at the edges are denoted by the red arrows in (d).

Note that the crack regions [displayed as red structures in Figs. S3(a & b)] almost disappear in Fig. S3(d), which justifies that our method can minimize the structure perturbations. However, because of the scanning drift and other factors (such as lattice expansion in PdH_x), it is not easy to precisely locate the edges of a sample, resulting in some image artifacts appear at the edges [denoted as red arrows in Fig. S3(d)].

S3. The relation between A_{th}, Z_{eff}, and hydrogen content (x)

The principle of ZEM is based on the empirical result shown in Fig. 1(c) of the main text. Because of A_{th}/A=98%, the measured A_{th} agrees with that of CASINO simulation very well. The result of Fig. 1(c) thus establishes a relation between A_{th} and Z_{eff}. For PdH_x, we can employ CASINO simulation to obtain the relation between A_{th}, $Z_{PdH}=(46+x)/(1+x)$, and x, as shown in Fig. S4(a). Similarly, the relation between $(A_{th}(PdH_x)-A_{th}(Pd)_0)/A_{th}(Pd)_0$ and x can be established as well, as shown in Fig. S4(b). Note that $A_{th}(Pd)_0$=0.696 denotes A_{th} of a pristine Pd, in which no hydrogen absorption has occurred.

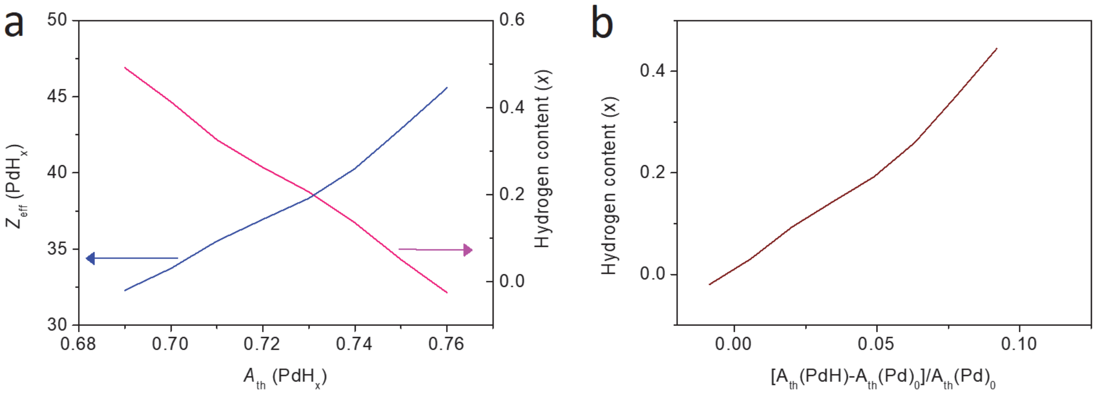

Fig. S4. The relation between A_{th}, Z_{eff}, and hydrogen content (x) (a) The relation between A_{th}, $Z_{PdH}=(46+x)/(1+x)$, and x. (b) The relation between $(A_{th}(PdH_x)-A_{th}(Pd)_0)/A_{th}(Pd)_0$ and x.

Although both A_{th} vs Z_{eff} and A_{th} vs x relations are approximately linear, the relation of Fig. S4 is used when estimating x in our data and no linear approximation is applied.

S4. Monte Carlo simulation of the absorbance of voids

The simulations are conducted using the CASINO Monte Carlo program (Version 3.3.0.4) using the MONSEL Defaults model[3]. The model incorporates the Browning approach for calculating the Mott elastic scattering cross-section and the Joy and Luo model[4,5], which has been further modified by Lowney[6] to calculate inelastic scattering energy loss (dE/dS). We typically input 100,000 electrons with various electron beam diameters and acceleration voltages (V_{acc} =1~20 KV). This enables us to obtain interaction volume, reflectance (R), transmittance (T), and total absorbance (A) based on the input parameters.

The defect density (ν_{eff}) determined by our ZEM method relies on the assumption that all vacancies are atomic scales, and its definition is to count how many atoms are missing, on average, from a unit cell. In reality, voids or cracks may exist in the samples, and the definition of the corresponding defect density would be dissimilar. To investigate their effects, we have employed CASINO simulations on arrays of voids in Si_3N_4 under electron beam irradiation, as shown in Fig. S5(a). We first obtain the A and follow the same guideline of our ZEM method to determine v_{eff}. Then we estimate how much volume of voids (V_{void}) is located within 90% of the interacting volume (V_{ebeam}) of the electron beam. The volumetric void concentration (D_{void}) is obtained by $D_{void} = V_{void}/V_{ebeam}$.

It must be pointed out that D_{void} may not be a well-defined quantity when employing an electron beam as a probe. Furthermore, the CASINO simulation would not be accurate when the void size becomes too small. Nevertheless, it is still worthwhile to know the difference between the two concentrations. Figure S5(b) shows their ratio (v_{eff}/D_{void}) for different void sizes. We find that v_{eff} tends to overestimate the void concentration by 150% when the void sizes are about 35nm, and the overestimation increases to 350% when the void size is reduced to 20nm.

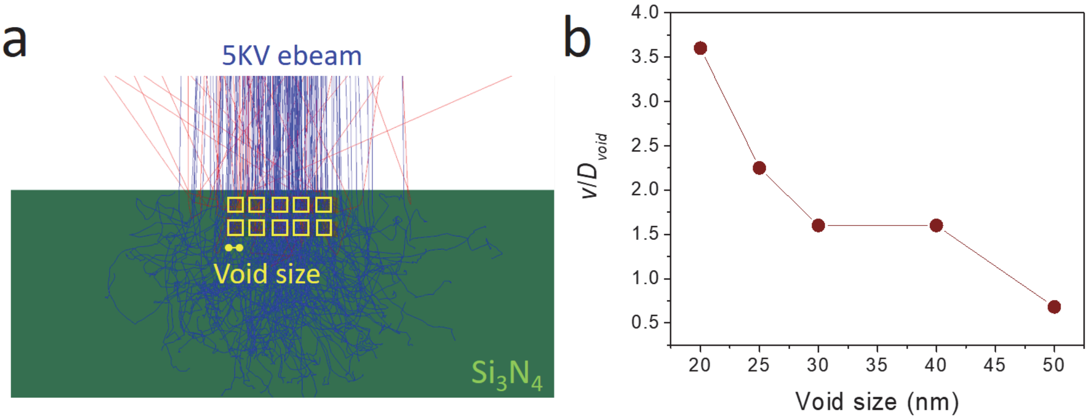

Fig. S5. CASINO simulation of an electron beam interacting with an array of voids. (a) Schematic illustration of a 5 KV electron beam interacting with a SiN_x sample with two layers of voids. (b) v_{eff}/D_{void} with different void sizes.

However, we emphasize that probing nanoscale voids and estimating their D_{void} are always difficult for conventional tools, including Archimedes' method, thermal differential method, Raman spectroscopy, PL spectroscopy, etc. Although D_{void} may be ill-defined at the nanoscale, the simulation results show that ZEM remains a valuable tool for estimating their abundance.

S5. The evolution of hydrogens and defects in Region II

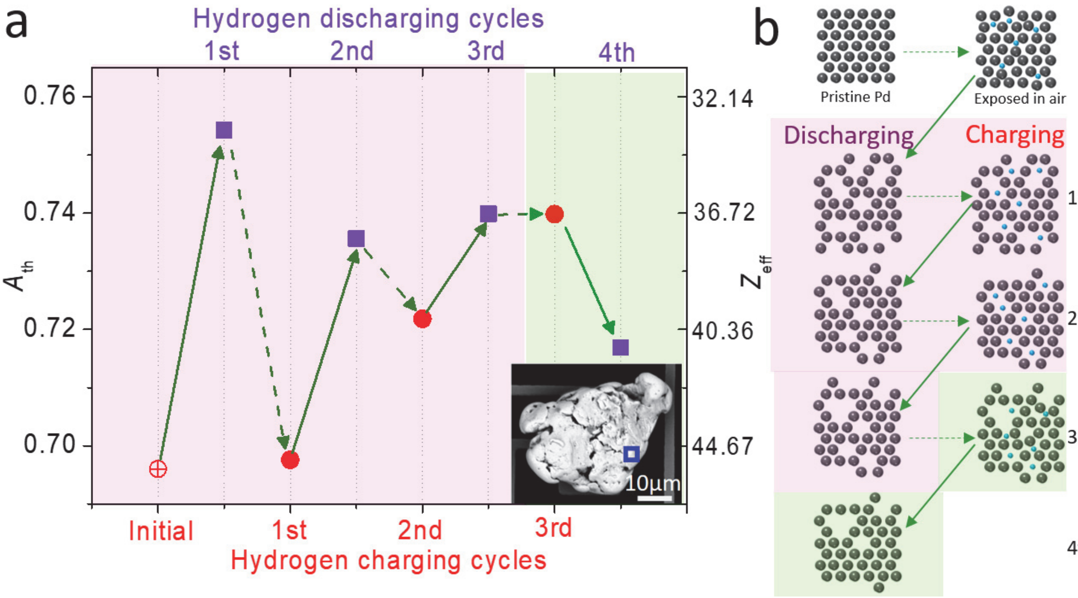

Fig. S6. The evolution of A_{th} in Region II. (a) The Region II is denoted in the blue area shown in the inset. The discharged and charged processes are respectively denoted as solid and dashed arrows, resulting in Pd (purple squares) or PdH_x (red circles). Because the A_{th} of a pristine Pd is not available here, the result from the CASINO simulation (A_{th}=0.696, denoted as an open-crossed circle) is used as a reference. The measurement uncertainties of A_{th} is estimated to be ±1%. (b) Schematic illustrations of the hydrogen uptake and defect formation processes during the charging-discharging cycles. Here, Pd and hydrogen atoms are denoted as dark gray and blue circles, respectively. The processes showing $A_{th}(Pd)>A_{th}(PdH)$ and $A_{th}(Pd)<A_{th}(PdH)$ are denoted by the shaded purple and green regions, respectively.

S6. The evolution of hydrogens and defects of another Pd micrograin

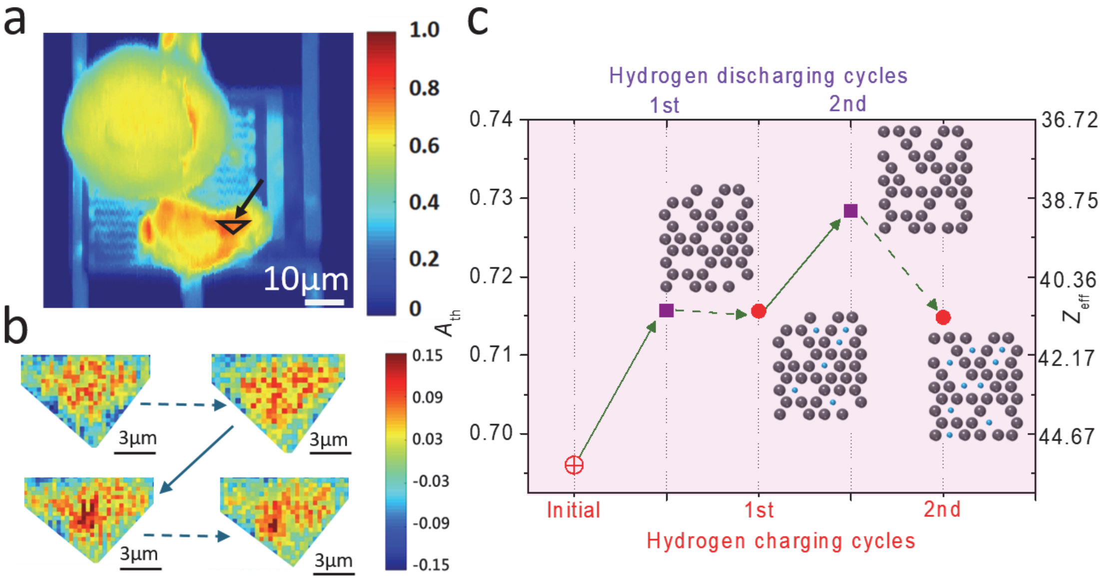

Fig. S7. The evolution of A_{th} of another Pd grain. (a) A ZEM image (identical to Fig. 2(c)) where a flat region of the Pd micrograin (denoted by the black arrow) is used for A_{th} analysis. (b) The evolution of $(A_{th}(PdH_x)-A_{th}(Pd))/A_{th}(Pd)$ of the selected region during two cycles of hydrogen discharging and charging, where A_{th}(Pd)=0.696 is determined by CASINO simulation. (c) The evolution of the averaged A_{th} of the selected area during the charging-discharging cycles. The measurement uncertainties of A_{th} is estimated to be ±1%. The schematic illustrations of the hydrogen uptake and defect formation processes are also shown in the insets. Unlike Fig. 3 of the main text, only A_{th}(Pd)>A_{th}(PdH) processes (denoted by the shaded purple) are found here.

S7. The electron beam's penetration depth (*d*) vs V_{acc}

The penetration depth (*d*) of an electron beam for a given V_{acc} has been analytically studied by Kanaya and Okayama[7], in which *d* (has unit in m) can be expressed by

$$d = \frac{0.0276 m_A N_A E^{5/3}}{Z^{8/9}\rho} \tag{1}$$

where E=eV_{acc} is the energy of electron in KeV, m_A is the atomic mass in kg, N_A is Avogadro's number, ρ is the density in kg/m^3. The *d* can also be obtained from Monte Carlo simulation by, for example, defining 10% of the incident electrons penetrate through a plane of *d* beneath the surface. Figure S8 shows the results of Eq. (1) and the CASINO simulation for Pt (Z_{Pt}=78). We can see that both methods are consistent with each other and their difference can be attributed to the different definitions of *d*.

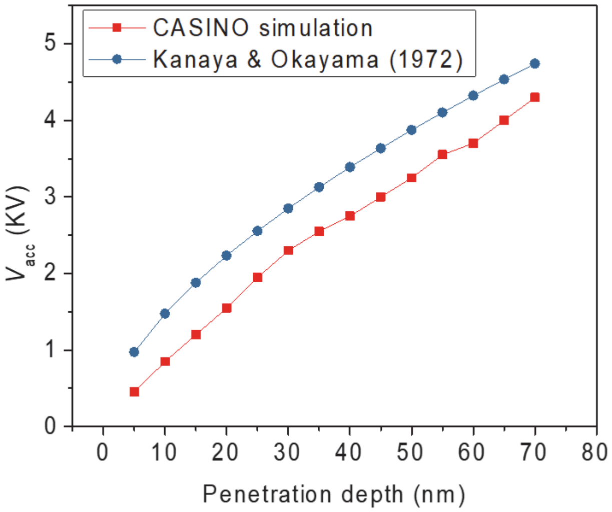

Fig. S8. The penetration depth (*d*) vs V_{acc} for Pt. Here the analytical results from Kanaya & Okayama[7] (dark blue circles) and CASINO simulation (red square) are shown for comparison. Their difference can be attributed to different definition of *d*.

The validity of Eq. (1) and the CASINO simulation have been experimentally verified by Yuan *et al*[2].

References

1. Lin, C. C.; Wang, S. M.; Chen, B. Y.; Chi, C. H.; Chang, I. L.; Chang, C. W. *Nano Lett.*

2022, 22, (7), 2667-2673.

2. Yuan, P. Y.; Wu, J. Y.; Ogletree, D. F.; Urban, J. J.; Dames, C.; Ma, Y. B. *Nano Lett.* **2020,** 20, (5), 3019-3029.
3. Demers, H.; Poirier-Demers, N.; Couture, A. R.; Joly, D.; Guilmain, M.; de Jonge, N.; Drouin, D. *Scanning* **2011,** 33, (3), 135-146.
4. Joy, D. C.; Luo, S. *Scanning* **1989,** 11, (4), 176-180.
5. Browning, R.; Li, T. Z.; Chui, B.; Ye, J.; Pease, R. F. W.; Czyzewski, Z.; Joy, D. C. *J. Appl. Phys.* **1994,** 76, (4), 2016-2022.
6. Lowney, J. R. *Scanning* **1996,** 18, (4), 301-306.
7. Kanaya, K.; Okayama, S. *J. Phys. D: Appl. Phys.* **1972,** 5, (1), 43.